Monthly Notices of the ROYAL ASTRONOMICAL SOCIETY

MNRAS **536,** 2072–2085 (2025) https://doi.org/10.1093/mnras/stae2680
Advance Access publication 2024 December 3

IFUM integrated field spectroscopy of ten M104 satellite galaxy candidates

Ethan Crosby ,[1]★ Mario Mateo,[2] Ivanna Escala ,[3] Helmut Jerjen,[1] Oliver Müller[4] and Marcel S. Pawlowski[5]

[1]*Research School of Astronomy and Astrophysics, Australian National University, Canberra, ACT 2611, Australia*
[2]*Department of Astronomy, University of Michigan, 1085 S. University Avenue, Ann Arbor, MI 48109, USA*
[3]*Department of Astrophysical Sciences, Princeton University, 4 Ivy Lane, Princeton, NJ 08544, USA*
[4]*Institute of Physics, Laboratory of Astrophysics, Ecole Polytechnique Fédérale de Lausanne (EPFL), CH-1290 Sauverny, Switzerland*
[5]*Leibniz-Institut für Astrophysik Potsdam, An der Sternwarte 16, D-14482 Potsdam, Germany*

Accepted 2024 November 22. Received 2024 October 25; in original form 2024 July 17

ABSTRACT

We report the spectroscopic analysis of 10 satellite galaxy candidates in the sphere of influence of the Sombrero galaxy (M104, NGC4594), based on data obtained with IFUM (integral field units for Magellan). Based on their newly observed recessional velocities, we confirm that nine of these candidates are satellite galaxies of M104, with one being a background dwarf galaxy. All 10 dwarfs have stellar masses 2×10^7 to $1 \times 10^9\,\mathrm{M}_\odot$ and mean weighted metallicities $-1.7 < \langle[\mathrm{M/H}]\rangle < -0.3$. Although these dwarfs are predominantly old, with stellar populations $\sim$ 5–11 Gyr. However, this sample contains a local example of a low-mass 'green pea' candidate, it exhibits extreme optical emission features and broad emission line features ($\sigma \sim 250\,\mathrm{km\,s^{-1}}$) reminiscent of high-redshift Ly α/Ly C photon leaking galaxies. Using the newly acquired recessional velocities of the nine satellites of M104, we find no evidence of coherent satellite motions unlike other nearby L_* galaxy environments. Given the small sample, this result does not statistically rule out such coherent motions. There remain 60 satellite candidates of M104 for which future spectroscopy can more reliably test for such motion. Using the observed dwarf galaxies as tracers of the gravitational potential of M104, we estimate the dynamical mass of M104, $M_{\mathrm{dyn}} = (12.4 \pm 6.5) \times 10^{12}\,\mathrm{M}_\odot$, and find that, making a reasonable estimate of M104's gas mass, $>$ 90 per cent of its baryons are missing. These results agree with previous measurements of M104's dynamical mass.

Key words: galaxies: distances and redshifts – galaxies: dwarf – galaxies: groups: individual: M104 – galaxies: kinematics and dynamics – cosmology: observations.

1 INTRODUCTION

Reconstruction of the satellite galaxy systems of the Milky Way and M31 with full 6D phase-space coordinates consisting of the on-sky positions, distances, line-of-sight (LOS) velocities and on-sky proper motions has revealed that these satellites are co-orbiting about their hosts in flattened, apparently stable structures known as satellite planes (Conn et al. 2013; Ibata et al. 2013; Pawlowski, McGaugh & Jerjen 2015; Pawlowski & Kroupa 2019; Pawlowski & Sohn 2021). Based on only positions and radial velocities, a similar configuration of satellites appears to exist around Centaurus A (Tully et al. 2015; Müller et al. 2018a, 2019; Müller et al. 2021), NGC253 (Martínez-Delgado et al. 2021), and NGC4490/NGC4485 (Karachentsev & Kroupa 2024). These empirical results for well-studied host galaxies in the local universe suggest that satellite planes may be common. In contrast, similarly coherent, flattened, and (apparently) stable structures are rarely seen in Lambda cold dark matter (ΛCDM) cosmological simulations which generally predict that satellites do not often have preferential spatial and kinematic orientations (Metz, Kroupa & Jerjen 2009a; Ibata et al. 2013, 2014; Müller et al. 2018a; Pawlowski & Kroupa 2019; Pawlowski 2021; Pawlowski & Sohn 2021).

Extensive research has been conducted to better understand the discrepancy. Cautun et al. (2015) highlighted statistical biases in the methods used to determine the significance of a plane, specifically the *look-elsewhere* effect. This occurs when apparently significant results are found purely by chance when evaluating a large parameter space, which may have produced a misleading level of significance in the evaluation of the Local Group satellite planes. Other conceivable biases exist that could explain coherent satellite structures. For example, one may argue unique formation conditions within the local cosmic environment (e.g. the Local Sheet: Tully et al. 2008) that hosts the best-studied galaxies with satellite planes to date favour the formation of coherent structures around nearby host galaxies. Libeskind et al. (2019) found a preferential global alignment of satellites within the Local Sheet, and other studies (Neuzil, Mansfield & Kravtsov 2020; Aragon-Calvo, Silk & Neyrinck 2022) are finding that the structure of the Local Sheet may be a cosmological outlier. These solutions mostly pertain to a class of physical processes, including galaxy accretion along flattened cosmic filaments (Libeskind et al. 2010; Lovell et al. 2011), group infall of dwarf galaxies (Metz et al.

★ E-mail: ethan.crosby@anu.edu.au

2009b; Vasiliev 2023) and interaction fragments, known as tidal dwarf galaxies, rotating in thin planes following galactic interactions (Kroupa, Theis & Boily 2005; Metz & Kroupa 2007; Kroupa 2012; Pawlowski, Pflamm-Altenburg & Kroupa 2012; Hammer et al. 2013; Bílek et al. 2018; Banik et al. 2022). Other potential solutions suggest that observed satellite planes are transient or unstable structures, based on searches for satellite planes within simulations (Bahl & Baumgardt 2014; Gillet et al. 2015; Buck, Dutton & Macciò 2016; Shao, Cautun & Frenk 2019). There are also a growing number of studies that suggest the satellite plane of the Milky Way is not a outlier in ΛCDM simulations when the dynamics of the Large Magellanic Cloud are considered (Garavito-Camargo et al. 2021; Samuel et al. 2021; Vasiliev 2023), though this specific explanation obviously does not directly apply to other systems where coherent dwarf structures are claimed to exist.

Questions that arise from this summary include: Which of these solutions represent 'normal' dwarf galaxy distributions? Does one specific bias or physical effect dominate as the source of the model/observation discrepancy, or are various factors simultaneously involved? Addressing these questions requires a broader range of observed systems that are located in a larger, more diverse region of space beyond the Local Volume. Aside from some recent pioneering efforts (Heesters et al. 2021; Karachentsev & Kroupa 2024), based on spatial distributions, few comprehensive studies of satellite systems beyond a few *Mpc* have been carried out to date. This has motivated searches for dwarf galaxy systems associated with hosts located well beyond the Local Volume and, so far, out to distances of up to 12 Mpc (Crnojević et al. 2016; Javanmardi et al. 2016; Müller et al. 2017; Müller, Jerjen & Binggeli 2018b; Byun et al. 2020; Danieli et al. 2020; Müller & Jerjen 2020; Carlsten et al. 2022; Crosby et al. 2023a, b). Extensive catalogues of dwarf satellite galaxy candidates out to this distance now exist as a result of these wide and deep optical surveys. But that is only the first step. Determining the presence or absence of a satellite plane requires full positional (membership) and kinematic information for these satellites.

The next crucial step to explore the frequency and general properties of satellite distributions – including the key question of whether satellite planes are ubiquitous – is to carry out spectroscopic follow-up of satellite candidates (Müller et al. 2021; Heesters et al. 2023). Spectroscopy serves three key purposes: (i) confirmation of candidates as true satellites of their assumed hosts; (ii) exploring the satellite kinematics about their hosts; (iii) discerning the metallicity, stellar content, and – in favourable cases, internal kinematics of satellite systems. These results help to distinguish true satellites from background galaxies and to look for possible co-rotation of satellites about their host, a key signature of satellite planes. Ultimately, such studies of newly discovered satellite systems also broaden the scope of interesting research questions, including determining how the morphology of the host galaxy may affect the prevalence of a satellite plane, whether satellite-plane membership of dwarfs correlates to star formation history (as expected in hierarchical formation), how dwarfs are internally affected by group membership, and whether larger-scale cosmic superstructures influence the formation of satellite planes (Pawlowski 2018; Libeskind et al. 2019).

In this paper, we present the initial results of an observational study of dwarf satellite candidates in the M104 group aimed at addressing these science goals. In Section 2, we introduce 10 dwarf satellite galaxy candidates identified photometrically near M104 and describe the use of IFUM (integral field units for Magellan) to study these systems spectroscopically. In Section 3, we present results of the observations on these ten candidates with IFUM, including an investigation of whether this sample reveals coherent satellite motions in the halo of M104, and a determination of the dynamical mass of M104 based on the kinematics of its dwarf galaxy population.

2 TARGET SELECTION

In a previous study (Crosby et al. 2023b), we searched for satellite galaxies within the virial radius of the Sombrero galaxy (M104, also known as NGC4594 or PGC42407) using deep CCD g-band images obtain with the Hyper Suprime-Cam (HSC) at the 8 m Subaru telescope. Combined with other imaging surveys conducted around M104 aimed at finding satellite galaxy candidates (Karachentsev et al. 2000; Javanmardi et al. 2016; Carlsten et al. 2020; Karachentsev et al. 2020; Crosby et al. 2023b), we can identify 75 dwarf satellite galaxy candidates within the virial radius of M104, complete to a magnitude limit of $M_g \sim -9.5$ or a surface brightness limit of $\mu_{0,g} \sim 27$.

This sample is ideal for follow-up spectroscopic or resolved and deep photometric observations to confirm how many are likely physical satellites of M104. Given that M104 is largely isolated from other L_* galaxies, systemic velocity measurements are not only a reliable means of confirming which of these dwarf galaxy candidates are associated with M104 but also provides a means of exploring whether any substructure, such as satellite planes, is present. The large size of the M104 sample has particular potential to greatly improve the statistical analysis of the system. Its isolation from other massive host galaxies creates an ideal setting to examine its satellite population to explore the satellite plane problem. These factors have motivated the spectroscopy follow-up in this paper.

M104 is a particularly well-suited for follow-up spectroscopy for a number of reasons. The galaxy resides at a reasonably close distance of 9.55 ± 0.34 Mpc (McQuinn et al. 2016) and has a distinct systemic recessional velocity of $v_\odot = 1095 \pm 5\,\mathrm{km\,s^{-1}}$. With a high peculiar velocity of $v_p \sim 300$–$400\,\mathrm{km\,s^{-1}}$, this places this galaxy well outside the Local Sheet as delineated by a line-of-sight (LOS) recessional velocity discontinuity in galaxies beyond ∼ 7–8 Mpc (Tully et al. 2008; McCall 2014; Karachentsev et al. 2015; Anand et al. 2019). Given the satellite planes associated with galaxies in the Local Sheet appear to align with the Local Sheet (Libeskind et al. 2019), M104 represents an interesting test case that should not be affected by this local cosmological structure. M104 is also spatially and kinematically distinct from the Virgo Cluster given its location well in the foreground of the cluster's southern extension by around 6–10 Mpc (Tully 1982; Kourkchi & Tully 2017) and M104's considerably lower systemic velocity compared to the mean redshift of Virgo. This firmly places M104 in a sparsely-populated 'bridge' between the Local Sheet and the core of the Virgo cluster. We list some of the basic characteristics of M104 in Table 1.

Prior to this work, only five of the 75 current dwarf galaxy candidates have been spectroscopically confirmed as satellites within the M104 virial radius limit; these system's properties are summarized in Table 2. Of the remaining 70 objects, 39 are classified by Crosby et al. (2023b) as 'high' probability M104 group members, while the remaining 31 are considered to be 'low' probability members.

This paper presents new spectroscopic results for 10 of these high-probability candidate group members (these are illustrated in Fig. 2). The data presented here were obtained with IFUM, a new instrument deployed at the Nasmyth-East focus of the 6.5m Magellan/Clay telescope at Las Campanas Observatory (Mateo et al. 2022). These 10 targets were selected to reasonably represent the diversity of dwarf galaxies found near M104, from vigorously star-forming blue compact dwarfs (BCDs), to quenched low surface brightness dwarf ellipticals (dEs). This variety of astrophysically interesting galaxies

Table 1. Basic parameters of M104.

Morphology	SA(s)a	Corwin, Buta & de Vaucouleurs (1994)
RA(J2000)	12:39:59.4	
Dec. (J2000)	−11:37:23	
$v_{\odot}$	1095 km s^{-1}	Tully, Courtois & Sorce (2016)
D_{25}	8.′7 = 24.2 kpc	Corwin et al. (1994)
Distance (TRGB)	9.55 ± 0.34 Mpc	McQuinn et al. (2016)[a]
$(m - M)$	29.90 ± 0.08	McQuinn et al. (2016)
$M_{B_T,0}$	−21.51 mag	Corwin et al. (1994)
$v_{\rm rot}^{\rm max}$	345 km s^{-1}	Schweizer (1978)
M_*	1.8 × 10^{11} M$_{\odot}$	Muñoz-Mateos et al. (2015)
M_{200}	7.8 × 10^{12} M$_{\odot}$	(Crosby et al. 2023b)
R_{200}	420 kpc	(Crosby et al. 2023b)

[a]Distance measurements from various techniques are given in table 2 of McQuinn et al. (2016).

was also chosen, in part, to help evaluate the performance of IFUM in observing faint, low-surface brightness systems. The sample was also chosen to ensure a relatively even distribution of satellites around M104 as an exploration of the kinematics of the dwarf–galaxy system surrounding M104, and to serve as a first attempt to detect the presence of a possible satellite plane, or other substructure, around M104.

3 OBSERVATIONS

IFUM consists of three distinct fibre-optic IFUs, each feeding 'MSpec', a double spectrograph also used by M2FS (Mateo et al. 2012). The three IFUs are HR (high resolution), STD (standard resolution), and LSB (low surface brightness). Each of the IFUs operates by placing high-precision lenslet arrays at the focal plane of the Magellan/Clay telescope. Each lenslet is comprised of laser-etched bi-convex hexagonal surfaces in a fused-silica substrate, which projects images of the telescope primary mirror (the system entrance pupil) on to the ends of precisely aligned optical fibres (see Mateo et al. 2022 for further general details). The fibres for each IFU can be placed at the focal surfaces of the double MSpec spectrograph which was originally constructed for use with the multifibre, wide-field fibre spectroscopy system M2FS (Mateo et al. 2012). The observations obtained for this study exclusively used the LSB IFU which we describe in further detail here.

The LSB IFU array consists of 360 individual lenslets in an 18 × 20 array (see the top left panel in Fig. 1). Each spaxel of the lenslet array has an effective diameter of 1.90 arcsec (this equals the diameter of a circle with the same area as the hexagonal elements of the LSB IFU). The LSB IFU spans a field of 32.7 arcsec × 31.4 arcsec. The LSB fibres have core diameters of 260 μm, and are about 3.2 m in length. Both (identical) spectrographs of MSpec are of quasi-Littrow design and hence project these fibres a 1 : 1 magnification on to a pair of 4096 × 4120 E2V CCDs with 15 μm pixels. The two CCDs each image 180 of the fibres from half of the spaxel array. The rows of individual spaxels defined by the lenslet array are transferred, in a zig-zag pattern, to the spectrograph CCD detectors as described in Fig. 1. During the observations reported in this paper, two fibres were dead on the R-side of the LSB IFU (see Fig. 1); these fibres have since been replaced.

Data for this paper were obtained over two observing runs in 2023 March and 2024 May. The 2023 March observations employed an 80 μm wide slit just behind the output ends of the fibres at the focal surfaces of the two identical spectrographs in MSpec. These data were obtained using 1 × 2 pixel binning (spectral × spatial) of the 4096 × 4112 CCD detectors. About 63 per cent of the light incident on the lenslet arrays was blocked by the 80-μm slits in this configuration. For the 2024 May run, the instrument set up was similar apart from using the 300-μm (full-open) slit which leads to no significant slit losses. The same binning (1 × 2) was employed as in 2023. All observations from both runs used the so-called blue 600 line/mm reflection gratings in MSpec which, with the 80- and 300-μm slits, delivered an effective spectral resolution of $R \sim 3600$ and $R \sim 1000$, respectively over a wavelength range of 4800–6700 Å. Table 3 indicates which slit configuration was used for each target (or just have two parts, one for LSB80 and one for LSB300). This setting comfortably spans from Hβ to Hα at the mean redshift of M104. By combining data from multiple spaxels we were able to obtain reliable absorption-line velocities of galaxies with mean surface brightnesses as faint as 24.5 mag/arcsec^2 in both configurations. Relevant details of the IFUM configuration used in this paper are summarized in Table 4.

Our primary science goal with these observations was to measure a reliable recessional velocity for each galaxy, coadding the spectra from each spaxel together as necessary. We eliminate the sky background from our spectra by exposing the IFU to empty sky, or a background target (BT) which we subtract from our science target (ST) frames. The total exposure time for each target was based on the galaxy's surface brightness and was selected to produce at least a measured bulk velocity for each galaxy. Observing details and basic structural parameters of each galaxy as reported in Crosby et al. (2023b) are provided in Table 3.

4 RESULTS

4.1 Spectral fitting

To produce our final spectra to measure systemic velocities, metallicities, weighted ages, and mass-to-light ratios, we co-added all spaxels of each galaxy, excluding spaxels that do not increase the signal-to-noise ratio when co-added, or which are clear foreground or background sources as determined typically from their radial velocities. In the unique case of LV J1235-1104, the spaxels containing the star formation regions were also excluded as unique spectral features (discussed further in Section 4.3.5) in these regions introduced significant fitting errors. The spaxels chosen to be co-added are shown for each galaxy in Fig. 2; the resulting IFUM spectra are shown in Fig. 3.

We employed the PYTHON implementation of the penalized PiXel fitting (PPXF) algorithm (Cappellari & Emsellem 2004; Cappellari 2016, 2023) that employs a penalized maximum-likelihood approach to fit stellar and gas spectral templates to the IFUM data to simultaneously extract recessional velocities, stellar ages, stellar metallicities, stellar mass-to-light ratios, and emission-line flux ratios. PPXF allows one to model a galaxy spectrum with superimposed stellar population synthesis (SPS) models with varying weights representing the spread in age and metallicity of the underlying stellar populations, and therefore the stellar mass-to-light ratio for the given galaxy.

For our analysis, we used the E-MILES SPS templates[1] (Vazdekis et al. 2016) with the following choice of parameters:

(i) The observation sample from the next-generation spectral library (NGSL), a library of spectra for 600 stars extending

[1]http://miles.iac.es/

Table 2. Basic parameters of the five existing confirmed satellite galaxies of M104. The table columns contain the following information: (1) galaxy name, (2) right ascension (J2000), (3) declination (J2000), (4) central *g*-band surface brightness, (5) mean *g*-band surface brightness within the effective radius, (6) reference for recession velocity.

Name (1)	RA (J2000) (2)	Dec (J2000) (3)	μ_0, g (g mag arcsec^{-2}) (4)	$\langle \mu_e, g \rangle$ (g mag arcsec^{-2}) (5)	$v_\odot$ (km s^{-1}) (6)	Reference (7)
UGCA287	12:33:55	−10:40:48	22.2	23.8	1052 ± 9	Corwin et al. (1994)
LV J1235-1104	12:35:39	−11:04:01	18.6	21.2	1124 ± 45	Jones et al. (2009)
PGC042120	12:37:14	−10:29:46	24.3	25.2	756 ± 2	Huchtmeier, Karachentsev & Karachentseva (2009)
SUCD1	12:40:31	−11:40:05	19.4	20.3	1293 ± 10	Hau et al. (2009)
PGC42730	12:42:49	−12:23:24	19.7	23.5	1025 ± 45	Jones et al. (2009)

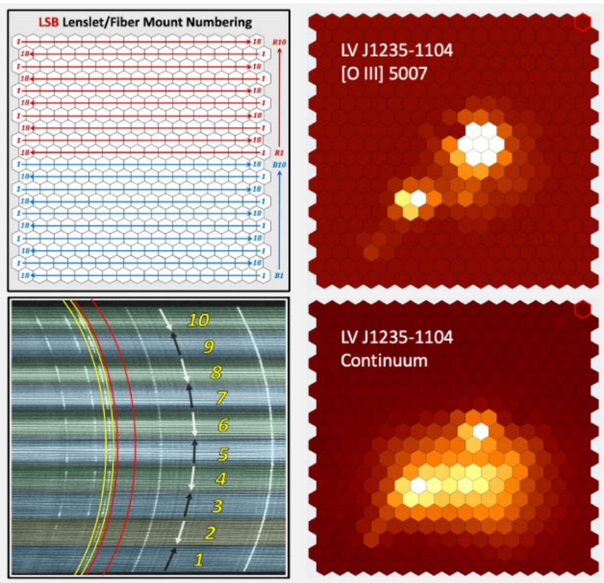

Figure 1. Top left: A schematic representation of the IFUM/LSB lenslet array as projected on to the sky with North to the top and East to the right when the Magellan/Clay Nasmyth-East rotator is at the home (zero) position. The fibres associated with the bottom half of the array feed the 'B' spectrograph while the upper half fibres feed the 'R' spectrograph (the two spectrographs are identical; the 'B' and 'R' notation is a relic from an earlier version of the instrument). The LSB fibres are mounted in groups of 18 fibres, 10 per spectrograph. The fibre mount notation and the fibre numbering is illustrated in this representation of the lenslet array. Note the zig-zag pattern of the fibre numbers. Bottom left: This shows a portion (about half) of the B-side CCD observations of LV J1235-1104 (discussed further in Section 4.3.5). The numerals refer to the 10 fibre mounts corresponding to the lower ten rows in the top left figure, each containing a set of 18 fibres. The arrows show the direction of constant direction, in this case from East to West when the instrument rotator is a the home position. Careful inspection of the galaxy emission lines (H β and [O III] 4959/5007 at left in this image shows how features alternate in orientation in successive fibre mounts. Upper right: An image of LV J1235-1104 based on the spectral region including only the [O III] emission line at 5007 Å (between the curved left-most lines in the lower left image). Lower right: An image of LV J1235-1104, this time sampling only the continuum radiation between the red arcs in the lower left image.

from 1660 to 10 200 Å acquired using *Hubble Space Telescope* (*HST*)/STIS[2].

[2]Compiled by Sara R Heap and Don Lindler: https://archive.stsci.edu/prepds/stisngsl/index.html

(ii) Theoretical scaled solar isochrones as described in Pietrinferni et al. (2004).

(iii) A bimodial $\Gamma_b = 1.3$ initial mass function (IMF) resembling the IMF proposed by Kroupa (2001).

(iv) The assumption that [M/H] = [Fe/H], implying that there is no enhancement of α-elements in the stellar spectra. This assumption is reasonable for dE galaxies similar to those observed in our programme (Geha, Guhathakurta & van der Marel 2003; Sen et al. 2017; Sen, Peletier & Vazdekis 2022).

Integrating the NGSL over (Pietrinferni et al. 2004) isochrones and the adopted IMF generates a series of SPS models whose free parameters are the age and metallicity of the stellar population.

For all our results, the templates are weighted by the mass of the constituent stellar population, which increases the sensitivity to older stellar populations that are less luminous than younger stellar populations but contain a greater proportion of the stellar mass of a galaxy. The alternative, using light-weighted templates, is strongly favoured towards younger stellar populations that when used to model dwarf starburst galaxies whose luminosity is dominated by young bright stars, may provide misleading mass-to-light ratios when a more massive but less luminous older stellar population is present. This is frequently the case in dwarf starburst galaxies (Zhao, Gu & Gao 2011) and thus why it is essential to use mass-weighted templates for star-forming galaxies.

We use the bootstrapping method as described in (Cappellari 2023) to better estimate uncertainties in the recessional velocity, metallicity, and stellar ages. This method involves perturbing the residuals of an initial singular fit to the spectra and re-fitting many times using the 'wild' bootstrapping method (Davidson & Flachaire 2008). We use 200 Monte-Carlo realizations for the results of each galaxy reported here. Additionally, we also use a regularization parameter of 3 for each galaxy to further smooth the results.

To calculate the stellar mass, we use the *i*- and *r*-band magnitudes as measured from DECaLS *i*- and *r*-band images (Zou et al. 2017, 2018), assuming the distance to M104 (or NGC4680 in the case of dw1244-1127) to calculate the luminosities and thus the stellar mass from the aforementioned mass-to-light ratio. We use the *i* and *r* bands, as it is less influenced by internal extinction and strong emission lines in star-forming galaxies than bluer pass bands.

An additional component that is sometimes required to model a galaxy's spectrum is the gas component, which, if present, can produce observable emission features if it is excited by energetic sources, e.g. star-forming regions. For this study, we have constructed a emission spectral template that contains the following strong emission lines found in the observed spectral range:

(i) H $\alpha\lambda$6563 and H $\beta\lambda$4861 Balmer series lines

Table 3. Basic structural and observing parameters of the 10 galaxies with IFUM spectroscopy reported in this paper. The table columns contain the following information: (1) galaxy name, (2) total science target (ST) time, (3) total background target (BT) time, (4) slit configuration, (5) observing pattern defined with the sequence of science target (S) and background target (B) frames, (6) right ascension (J2000), (7) declination (J2000), (8) central surface brightness, (9) mean g-band surface brightness within the effective radius, (10) morphological type, and (11) half-light radius from the underlying LSB component, ignoring nuclei, and star-forming regions, assuming a distance to M104, 9.55 Mpc (McQuinn et al. 2016), except for dw1244-1127 which we assume the distance to NGC4680, 30.1 Mpc (Tully et al. 2015). All structural parameters are from Crosby et al. (2023b).

Name	ST time (s)	BT time (s)	Slit (μm)	Observing Pattern	RA (J2000)	Dec. (J2000)	μ_0, g (g mag arcsec^{-2})	$\langle\mu_e, g\rangle$ (g mag arcsec^{-2})	Morph Type	r_e kpc
(1)	(2)	(3)	(4)	(5)	(6)	(7)	(8)	(9)	(10)	(11)
2023 targets										
UGCA287	2700	2400	80	B-S-S-S-B	12:33:55	−10:40:48	22.2	23.8	dIrr	1.42
LV J1235-1104	7200	4800	80	S-B-S-B-S	12:35:39	−11:04:01	18.6	21.2	BCD	0.28
KKSG31	6300	3900	80	B-S-S-S-B	12:38:33	−10:29:24	21.3	25.4	N-dE	1.12
dw1239-1143	16 500	9600	80	S-B-S-S-B-S-S-B-S-S-B	12:39:15	−11:43:08	22.2	24.4	N-dE	0.73
dw1239-1240	4500	2400	80	B-S-S-S-B	12:39:30	−12:40:30	22.2	24.7	N-dE	0.82
dw1240-1118	13 200	8700	80	B-S-S-B-S-S-B-S-S-B	12:40:09	−11:18:50	21.3	23.8	N-dE	0.72
dw1244-1127	4800	1200	80	S-B-S	12:44:38	−11:27:11	20.6	24.1	dIrr	1.96
2024 targets										
dw1233-0928	2700	1800	300	B-S-S-S-B	12:33:51	−9:28:08	21.1	23.5	dIrr	0.87
PGC42730	2700	1800	300	B-S-S-S-B	12:42:49	−12:23:27	19.7	23.4	N-dE	1.60
dw1245-1333	4500	1800	300	B-S-S-S-B	12:45:55	−13:32:31	22.9	24.6	dE	0.45

Table 4. IFUM instrumental parameters.

Parameter	Units	Value
LSB array size	arcsec	32.7 × 31.4
LSB array size	spaxels	20 × 18
Effective area	arcsec^2	1027
Spaxel diameter[a]	arcsec	1.90
Slit width	μm	(80)/(300)
Wavelength range	Å	4800–6700
Effective resolution	$\lambda/\Delta\lambda$	(3600)/(1000)

[a]The spaxel effective diameter is defined as $2\sqrt{A/\pi}$, where A is the nominal area of a single hexagonal spaxel of the LSB IFU. Values with format (x)/(y) indicate changes between the 2023 and 2024 observing runs, respectively.

(ii) [OIII]λ4959 and λ5007 doublet
(iii) He Iλ5876
(iv) [OI]λ6300 and λ6369 doublet
(v) [NII]λ6548 and λ6584 doublet

The relative ratios of these lines are allowed to vary as often seen in spectra of star-forming galaxies. We use the measured ratios of the H β and H α emission features to estimate the gas attenuation, from the Balmer decrement and case B recombination (Storey & Hummer 1995). Using equations (23a, b) and (c) from Cappellari (2023) for a generic extinction curve, we can thereby estimate the attenuation at any wavelength in our spectra.

To calibrate our spectra to physical units, we first convolve the DECam r-band filter with the optimal PPXF fit for the dEs dw1239-1143, dw1239-1240, and dw1240-1118 to simulate a DECam r-band magnitude. Then, we used the absolute magnitude as calculated from DECaLS r-band images (Zou et al. 2017, 2018) as described above. The SFR can be estimated from the calibrated H α intensity (Calzetti et al. 2007):

$$\mathrm{SFR}(\mathrm{M_\odot\,yr^{-1}}) = 5.3\times10^{-42}\,L(\mathrm{H}\,\alpha)_{\mathrm{corr}}\,(\mathrm{erg\,s^{-1}}), \quad (1)$$

where $L(\mathrm{H}\,\alpha)_{\mathrm{corr}}$ is correct for extinction. The SFR for each galaxy is provided in Table 5, as calculated from the co-added flux from all spaxels containing a H α signal.

For each galaxy spectra, we calculate the signal-to-noise ratio (SNR) using the following equation:

$$\mathrm{SNR} = \langle \mathrm{ST(Å)}\rangle \,/\, \sqrt{\langle \mathrm{BT(Å)}\rangle * \chi}, \quad (2)$$

where ST and BT represent the science target and the background target frames, respectively. χ comes from the PPXF fitting parameters and represents the quality of the fit. To avoid the influence of emission and absorption features, we select a 200 Å region from about 5950 – 6150 Å that is largely free of spectral features to make this comparison, thus effectively measuring the SNR of the continuum signal. The SNR for each galaxy is provided in Table 5.

4.2 Satellite membership

Critical to testing the hypotheses central to our science goals is confirming the membership of the dwarf galaxies presented in the paper as satellites of M104. A quantitative method to achieve this involves modelling the escape speed of the M104 halo as a function of radius from its centre. The LOS velocity of any satellite that significantly exceeds the escape speed at a given projected radius can be confidently excluded as a satellite of the M104 system.

To carry out this analysis, we assume that the M104 halo is spherically symmetric and that it can be reasonably modelled with an Einasto potential, $\phi_e(\mathrm{R})$, as formulated by Retana-Montenegro et al. (2012) (see equation 19).

Assuming that the M104 halo is spherically symmetric, we model the gravitational potential of the M104 system using the Einasto potential as formulated in equation 6b from Miller et al. (2016):

$$\phi(r) = \frac{-GM}{r}\left[1 - \frac{\Gamma\left(3n, \frac{r}{r_0}^{(1/n)}\right)}{\Gamma(3n)} + \frac{r}{r_0}\frac{\Gamma\left(2n, \frac{r}{r_0}^{(1/n)}\right)}{\Gamma(3n)}\right]. \quad (3)$$

We have adopted an Einasto index of $n = 3$ and a scale radius of 250 Mpc. These parameters provide a rotation curve that is a reasonably flat extrapolation of the inner rotation curve (Faber et al. 1977; Lewis 1985) out to the virial radius of M104 and given the mass from Section 4.5. We acknowledge the circular logic involved wherein by the mass of M104 is influenced by the choice to include certain dwarf galaxies in the method in Section 4.5, but the mass of M104 calculated here is

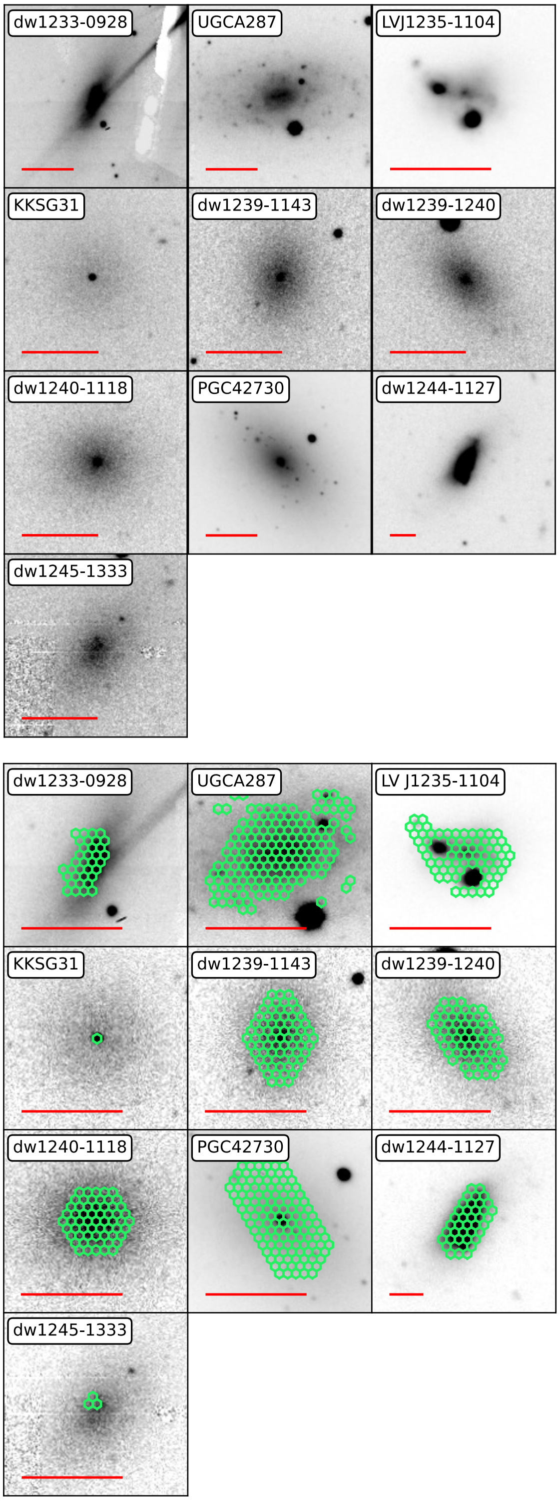

Figure 2. Upper frame**:** DECaLS *g*-band images (Zou et al. 2017, 2018) of our IFUM spectroscopy targets, north is up and east to the left. The horizontal bar at the bottom of each image represents a length of 1 kpc at the distance of M104. Lower frame: As the upper frame, but overlaid with hexagons indicating the spaxels considered to a part of the galaxy for the purposes of co-adding spectra to measure a bulk velocity for each galaxy. Some spaxels from galaxies are excluded when the spaxels are dead, the SNR of the spectra is too low, or it is otherwise affected by noise or foreground objects.

consistent with independent measurements, such as in Karachentsev et al. (2020) and the satellite membership of the dwarf galaxies is not strongly affected by variation in these parameters. Given the potential $\phi_e(\mathrm{R})$, the escape velocity as a function of radius is

$$v_{\mathrm{esc}}(r) = \sqrt{2 \times \phi_e(\mathrm{R})}. \tag{4}$$

We plot the escape velocity cone as a function of radius in Fig. 5, along with the recessional velocities of M104 dwarf satellite candidates including those from this paper. We find that with the exception of dw1244-1127 (which as illustrated in Fig. 10 is most likely a satellite of the background host galaxy NGC4680), that all the dwarf candidates are realistic satellites of M104 as they lie within the escape velocity cone.

4.3 Individual galaxies

4.3.1 KKSG31

KKSG31 is a nucleated dE for which we were only able to extract a reliable spectrum from the nuclear star cluster (NSC; Fig. 2) from which we obtain a recessional velocity $v_\odot = 1297 \pm 7\,\mathrm{km\,s^{-1}}$. We measure a mean mass-weighted metallicity of $\langle[M/H]\rangle = -1.4$ and a mean weighted age of 6.5 Gyr, within expectations for dE galaxies of this luminosity. The low S/N of 2.2 in the spectrum of KKSG31's NSC means we cannot fully resolve the relevant metal absorption features [Mg B (λ5205 and λ5193) and Na D (λ5980 and λ5985)]. The spread in metallicities shown in Fig. 4 for KKSG31 is the result of an upper limit on the intensity on those metal lines.

4.3.2 dw1245-1333

dw1245-1333 is the only non-nucleated dE in our sample and hence has too low an SNR for a reliable estimate of its population parameters from its continuum spectrum. Thus, we do not report stellar metallicities or ages for this galaxy. However, we did detect a weak emission signal in this galaxy localized to a small region offset from the galactic centre (as shown by the spaxel selection in Fig. 2), whose spectra suggests it is a small star-forming region. We used the emission signal from this star formation region to measure a recessional velocity of $v_\odot = 981 \pm 1\,\mathrm{km\,s^{-1}}$for this galaxy. The presence of this star-forming region might better classify this galaxy as a transitional dwarf galaxy (dT) or a dwarf irregular (dIrr).

4.3.3 dw1240-1118, dw1239-1143, dw1239-1240, and PGC42730

dw1240-1118, dw1239-1143, dw1239-1240, and PGC42730 are all nucleated dEs, possessing NSC. Interestingly, dw1240-1118 and dw1239-1143 both have higher recession velocities, of 1617 $\mathrm{km\,s^{-1}}$and 1378 $\mathrm{km\,s^{-1}}$, respectively, which is redshifted relative to M104 by 516 and 283 $\mathrm{km\,s^{-1}}$. However, the escape velocity cone in Fig. 5 suggests these galaxies are still bound to M104. We conclude that all three galaxies are satellites of M104.

The SNR for PGC42730's nucleus and surrounding galaxy spectra (18.9 and 46.9, respectively) are high enough that we can identify variations in the star formation history within this galaxy. As shown in Fig. 6, while both the nucleus and the rest of the galaxy have similar metallicity, a continuous range of younger stars in the nucleus suggests a scenario where ongoing star formation built up the nucleus *in situ* until around ~ 1 Gyr ago. The stellar mass of

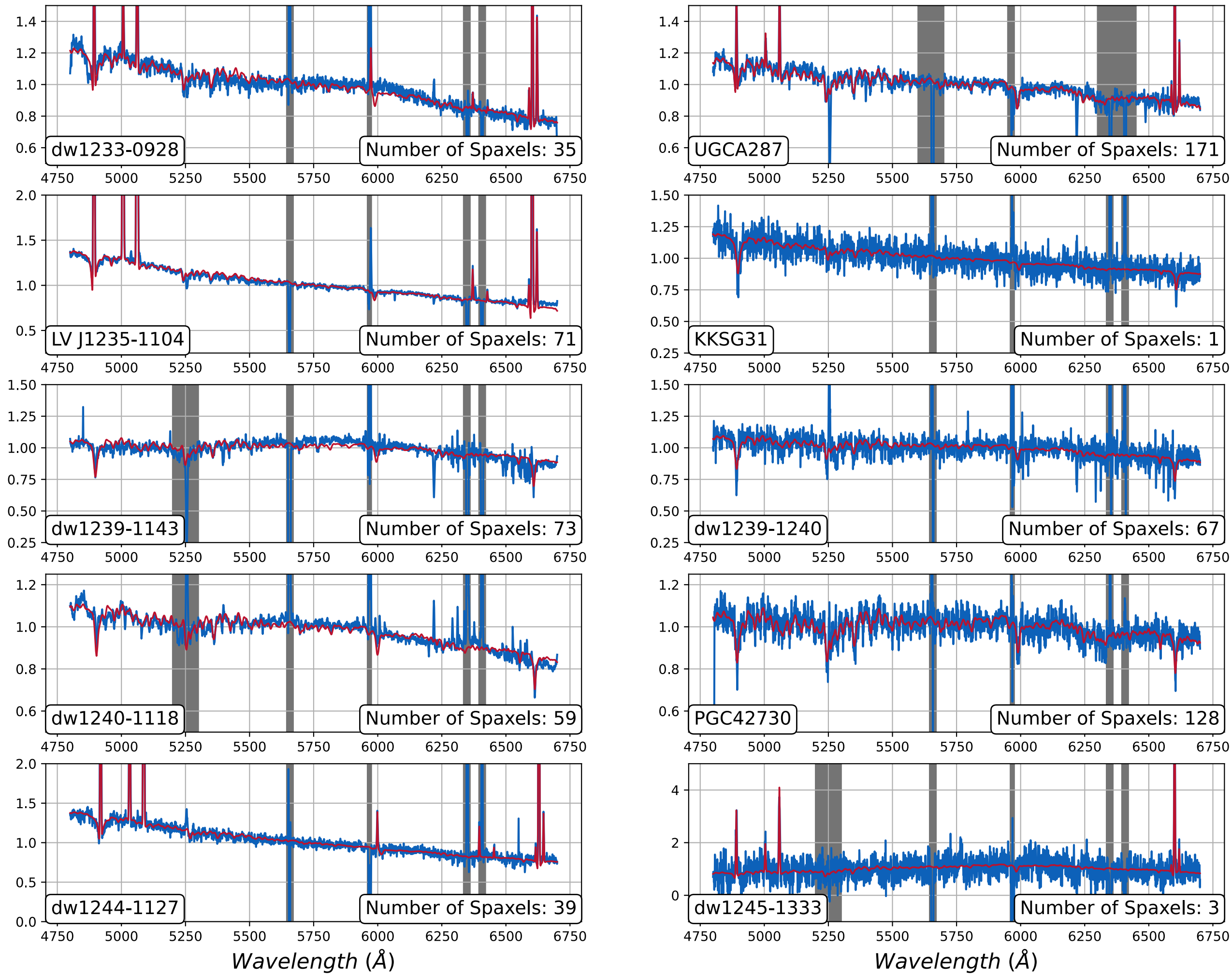

Figure 3. The co-added and continuum normalized IFUM spectrum for each target galaxy (blue line). The red line indicates the best PPXF fit from the stellar and gas templates. Greyed out windows are masked wavelength regions excluded from the fit due to the presence of saturated sky emission lines. The y-axis is an arbitrary normalized unit a function of erg s^{-1} cm^{-2} Å^{-1}. Each panel notes how many spaxels were co-added to produce the displayed spectrum.

Table 5. Kinematic and stellar population parameters of the 10 satellite galaxy candidates derived from galaxy spectrum. The columns contain the following information: (1) galaxy name, (2) mass-weighted stellar age, (3) mass-weighted stellar metallicity, (4) SFR calculated from H$_\alpha$ luminosity, (5) heliocentric velocity, (6) heliocentric velocity difference between the satellite and M104, (7) stellar mass, (8) number of spaxels used in building the galactic spectra shown in Fig. 3, (9) continuum signal-to-noise ratio of each resulting spectra. The heliocentric velocity of M104 is 1095 ± 5 km s^{-1} (Tully et al. 2016). The weighted age and metallicity are calculated from the weighted sum of the histograms in Fig. 4.

Name (1)	⟨age⟩ (Gyr) (2)	⟨[M/H]⟩ (dex) (3)	H$_\alpha$ SFR (M$_\odot$ yr^{-1}) (4)	$v_\odot$ (km s^{-1}) (5)	$\Delta v_{\odot,M104}$ (km s^{-1}) (6)	M_* ($10^7 \times$ M$_\odot$) (7)	# spaxels (8)	SNR (9)
				2023 targets				
UGCA287	$9.3^{+1.3}_{-4.2}$	$-0.5^{+0.2}_{-0.2}$	0.0013	1001 ± 1	-94 ± 5	53^{+6}_{-7}	171	38.7
LV J1235-1104	$8.5^{+2.7}_{-2.4}$	$-1.7^{+0.6}_{-0.4}$	0.042	1074 ± 1	-17 ± 5	$8.4^{+2.7}_{-1.8}$	71	61.3
KKSG31	$6.5^{+3.1}_{-1.9}$	$-1.4^{+0.3}_{-0.3}$	0.0	1309 ± 22	214 ± 23	$2.8^{+0.7}_{-0.6}$	1	2.2[a]
dw1239-1143	$9.0^{+0.8}_{-0.7}$	$-1.2^{+0.1}_{-0.1}$	0.0	1367 ± 12	272 ± 13	$4.9^{+0.7}_{-0.4}$	73	18.3[a]
dw1239-1240	$8.7^{+1.6}_{-1.3}$	$-1.2^{+0.3}_{-0.3}$	0.0	1040 ± 13	-55 ± 14	$7.9^{+0.5}_{-0.5}$	67	7.6[a]
dw1240-1118	$9.0^{+0.9}_{-1.0}$	$-0.9^{+0.1}_{-0.1}$	0.0	1593 ± 9	498 ± 10	$8.0^{+0.9}_{-0.3}$	59	31.8
dw1244-1127	$5.4^{+2.7}_{-1.1}$	$-1.3^{+0.9}_{-0.6}$	0.035	2441 ± 1	1346 ± 5	29^{+15}_{-5}	39	16.2[a]
				2024 targets				
dw1233-0928	$2.7^{+2.3}_{-1.1}$	$-0.3^{+0.4}_{-0.5}$	0.0016	1137 ± 2	42 ± 6	$9.8^{+4.9}_{-3.4}$	35	36.2
PGC42730	$10.9^{+1.3}_{-0.8}$	$-0.5^{+0.1}_{-0.1}$	0.0	1154 ± 4	59 ± 7	98^{+8}_{-7}	128	50.5
dw1245-1333	–	–	3.6×10^{-5}	981 ± 1	-114 ± 5	–	3	0[a]

[a]The SNR of these spectra are <20, thus the mean age and metallicities provided may be biased Woo et al. (2024).

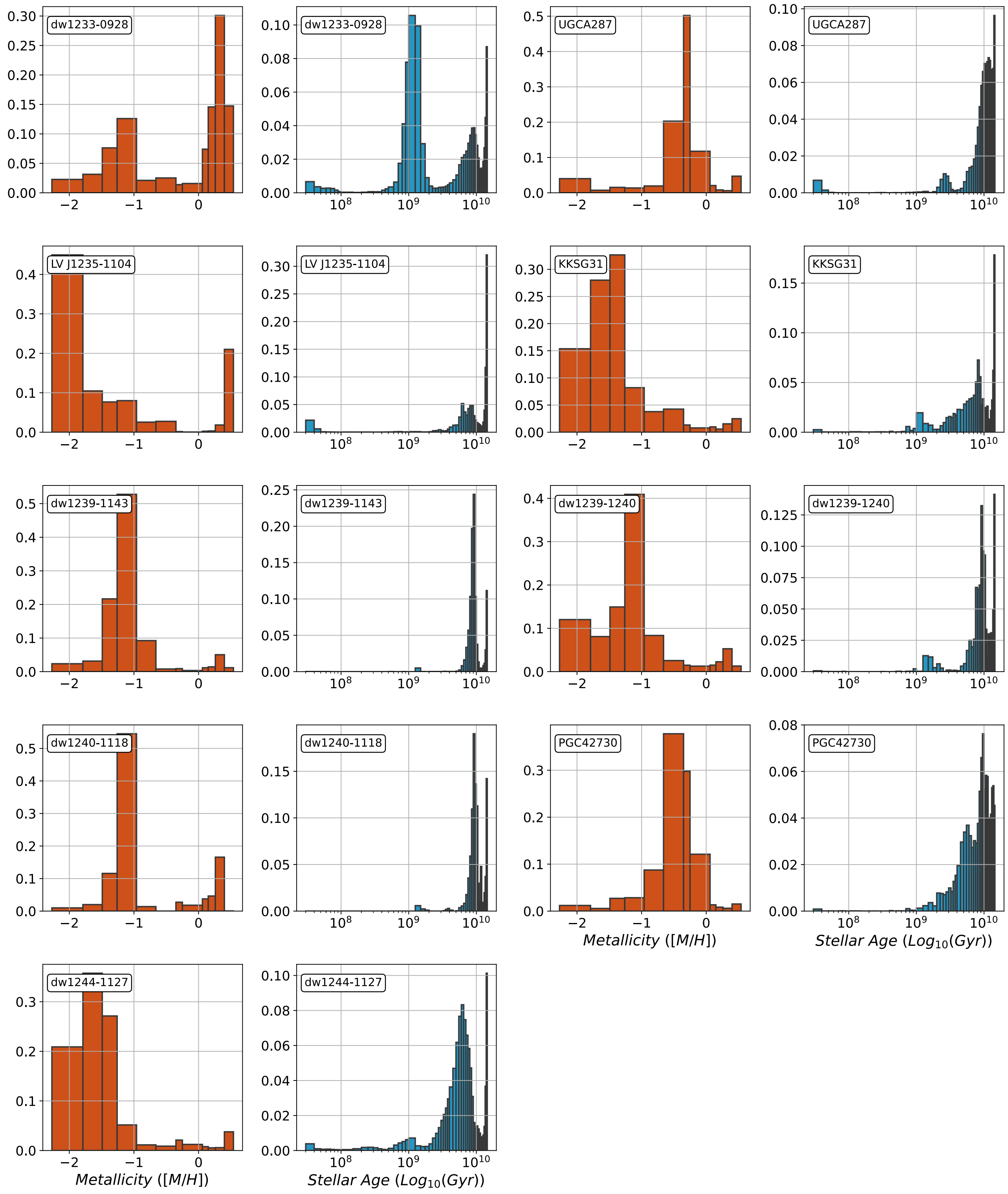

Figure 4. The normalized weights for the metallicity and stellar age of the E-MILES SPS templates fit to the data IFUM galaxy spectra by PPXF.

the nucleus is $M_* = 1.1 \pm 0.2 \times 10^7\,\mathrm{M}_{\odot}$, which means the fraction of stellar mass that resides in the nucleus is 0.01–0.02. This is expected for a galaxy of PGC42730's stellar mass, and matches the properties of NSCs found in other galaxies of this mass (Fahrion et al. 2022).

4.3.4 UGCA287 and dw1233-0928

UGCA287 and dw1233-0928 are both typical dwarf irregular galaxies with recessional velocities $v_{\odot} = 1000 \pm 1\,\mathrm{km\,s^{-1}}$and $v_{\odot} = 1137 \pm 2\,\mathrm{km\,s^{-1}}$, respectively. These galaxies are both large, with effective radii $r_e \sim 0.5$ and $r_e \sim 0.33$ arcmin, respectively (1400 pc

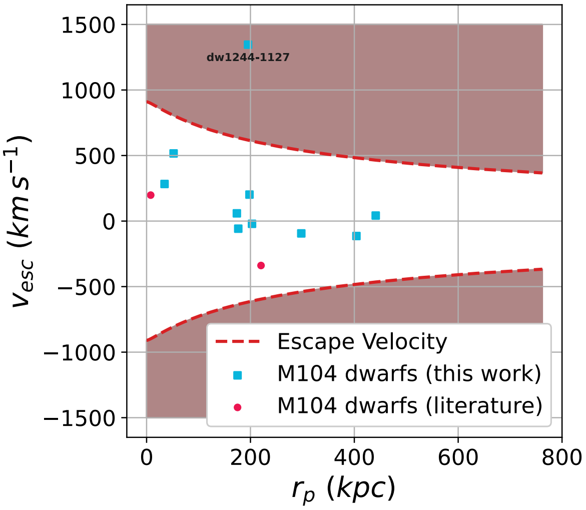

Figure 5. The escape velocity from the M104 halo (v_{esc}) as a function of projected radius (r_p) plotted with a dashed line. All spectroscopically measured M104 satellite velocities in this paper are plotted with squares, while velocities sources from elsewhere in the literature are represented with circles. dw1244-1127 is labelled separately in the plot and lies inside the shaded area which exceeds the escape velocity of the M104 system, and thus is not a satellite of M104.

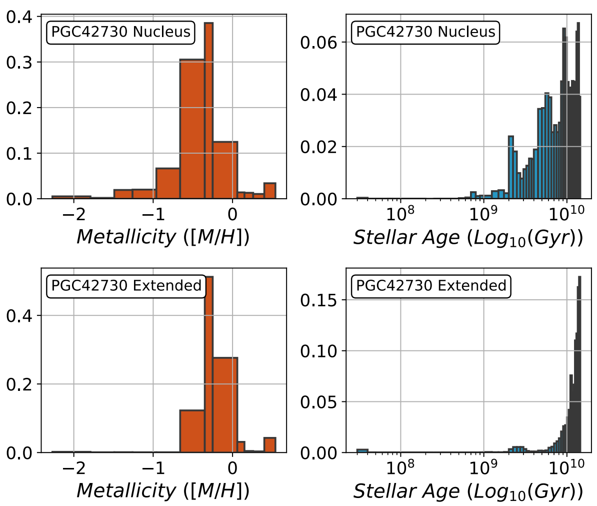

Figure 6. The stellar metallicity and age parameters for the stellar population of the nucleus (top row) and the rest of the galaxy, or the extended component (bottom row) for the nucleated dE PGC42730. The ongoing star formation up to $\sim$ 1 GYR ago in the nucleus suggests an *in situ* formation scenario for this nuclear star cluster.

and 900 pc at the distance of M104), parts of the galaxy extends beyond the field of view of IFUM. dw1233-0928 consists of two constituent stellar populations split into a bimodal metal rich and metal-poor population (as shown in Fig. 4). These dwarf irregulars have SFRs of 0.0013 and 0.0016 $M_\odot\ yr^{-1}$, respectively, but the SFR for UGCA287 may be underestimated as all star-forming regions were not captured within the IFUM field of view.

4.3.5 LV J1235-1104

LV J1235-1104 is a low-mass BCD ($M_* = 8.4 \times 10^7\ M_\odot$) and a candidate green pea (GP; Cardamone et al. 2009) galaxy. The

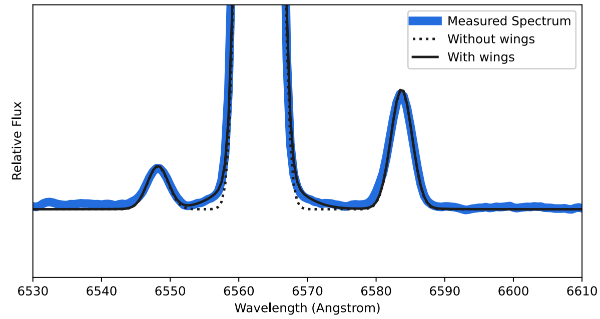

Figure 7. The line profiles of the Balmer H α transition and nearby nitrogen and oxygen forbidden transitions from the co-added spectra of LVJ1235-1104, shown with the tricker line. The fits to all three emission features are shown without Gaussian wings (dotted line) and with Gaussian wings (solid line). The 'wing' component is consistent with an ionized galactic wind with velocity $\sim$ 250 km s^{-1}.

classical GPs as originally reported in Cardamone et al. (2009) have stellar mass $M_* \sim 10^{8.5} - 10^{10}\ M_\odot$, making a LV J1235-1104 a low-mass Green Pea candidate, that some call a 'blueberry' (Yang et al. 2017; Liu et al. 2022). BCD and GP galaxies are both rare classes of galaxies (Lee et al. 2009; Karachentsev & Kaisin 2020) that are effectively dwarf starburst galaxies. Both classes are described purely by the colours and shapes of the galaxies in telescope images, both being compact and blue or green in colour, indicative of strong [O III] 5007 Å emission (Cardamone et al. 2009). Indeed, this emission line within LV J1235-1104's integrated spectra has a very large equivalent width of 314 Å that falls above the threshold of an extreme emission-line galaxy (EELGs) as defined in Amorín et al. (2015) (EW[O III]> 100 Å), which as a broad category include GP galaxies. EELGs are dominated by young stellar populations with high specific SFRs (sSFR$\sim 1 - 100 \times 10^{-9}$ yr^{-1}) and low mean metallicity (log[O/H] + 12 $\sim$ 8; Yang et al. 2017). Thanks to recent discoveries from *JWST* research programmes these galaxies have been shown to closely resemble the first galaxies of the universe (Curti et al. 2022; Harish et al. 2022; Taylor, Barger & Cowie 2022; Rhoads et al. 2023; Trump et al. 2023). Curiously, while the EW of the emission features in LV J1235-1104 are indicative of extreme star-forming conditions akin to these high-redshift dwarf starburst galaxies, its sSFR (sSFR $\sim 5 \times 10^{-10}$ yr^{-1}) is lower than the typical definition of an EELG. Modern ($z \sim 0$) starburst dwarf galaxies are distinct from high-z galaxies in that they often contain a population of older stars (Amorín et al. 2007, 2012), which contains > 90 per cent of the stellar mass of the galaxy. Earlier galaxies, which have not yet had the time to form an older population of stars, might therefore have a systematically higher sSFR, even among galaxies of comparable star-forming conditions and thus may account for the unexpectedly low sSFR in LV J1235-1104.

Additionally, recent IFU observations of GPs show they exhibit unique characteristics. They are intensely star-forming galaxies and are frequently Lyman continuum (Ly C) and Lyman alpha (Ly α) emitters (Izotov et al. 2017, 2018; Komarova et al. 2021; Malkan & Malkan 2021; Flury et al. 2022) and have a broad-line component of spectral emission features with $\sigma \sim$ 100–300 km s^{-1}(Bosch et al. 2019; Hogarth et al. 2020; Komarova et al. 2021). We have confirmed the presence of similar broad emission features in this galaxy as shown Fig. 7. These features originate from excited gas accelerated to high velocities. The source of this acceleration must be related to star formation, likely the radiation pressure from super-star clusters, which is expected to dominate over thermal pressure (Krumholz &

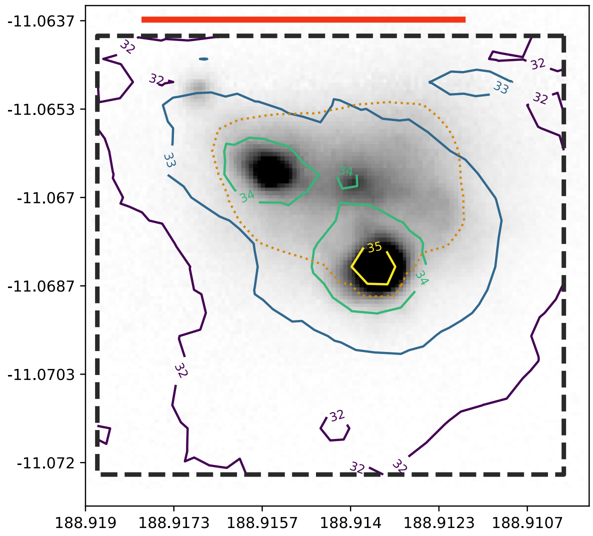

Figure 8. A contour plot of the H α emission intensity across the IFUM field of view, bounded by the thick dashed line. The horizontal thick line above the IFUM FOV represents a distance of 1 kpc at the distance of M104. The numbers superimposed on the contours represent the H α emission surface brightness with units of log (erg s^{-1} pc^{-2}), assuming the distance to the galaxy is 9.55 Mpc. The dotted contour represents the area containing the > 99 per cent of the stars within this galaxy.

Matzner 2009). Secondly, Komarova et al. (2021) ruled out a scenario where radiation pressure acting on the dust grains is responsible for the observed high velocity wind: the dust opacity must be around 2 orders of magnitude higher than even in a solar metallicity system in order to accelerate the gas to these high velocities. Among the only absorption mechanisms which has enough opacity to produce these high winds is Ly α/Ly C absorption of neutral hydrogen. Komarova et al. (2021) concluded that provided Ly α/Ly C photons are able to escape the star-forming regions, this is a viable explanation for these high velocity, star-formation−driven winds. This provides evidence that LV J1235-1104 is a Ly α/Ly C emitter like higher redshift GPs, but further observations such as direct UV spectroscopy with *HST*/COS is required to confirm this hypothesis.

We also detect the presence of a star-formation powered outflow of hot, ionized gas from an extended envelope of optical emission features in the circumgalactic medium (CGM). In Fig. 8, we show the H α emission surface brightness contour plot, which reveals the extended emission envelope that extends beyond the Stellar component of the galaxy, indicating that excited gas is being ejected from the star-forming regions into the CGM. Galactic outflows with outflow velocities that exceed the escape velocity of the host halo are common in low-mass BCD galaxies (Romano et al. 2023).

Low-mass dwarf galaxies have low rotational velocities and low escape speeds, such that feedback resulting from star formation or environmental interactions such as ram pressure stripping are thought to remove their star-forming gas reserves rapidly (Wetzel, Tollerud & Weisz 2015; Simpson et al. 2018; Garrison-Kimmel et al. 2019; Putman et al. 2021). This is supported with observational evidence, star-forming dwarf galaxies are much more common in the field, rather than inside of satellite galaxy systems, suggesting they are rapidly quenched in the presence of L_* host galaxies or that the mechanisms powering their intense star formation is strongly suppressed in satellite galaxy environments. Interactions between low-mass dwarfs and an L_* host galaxy quench starburst episodes as opposed to triggering them (Brunker et al. 2022; Laufman et al. 2022). LV J1235-1104 is both likely experiencing strong internal star formation feedback and environmental stripping from M104 (a projected distance of 200 kpc to M104) which given its low-mass indicates it will soon be stripped of its star-forming gas. Additionally, given its very low relative velocity ($\Delta v_{\odot, M104} = -20\,\mathrm{km\,s^{-1}}$), it must either be orbitting M104 in the plane of the sky or near its orbital apoapsis. Given that this galaxy still possesses its star-forming gas, the later scenario is likely, indicating that this galaxy is on its first infall into the M104 group.

For the results presented in Table 5, we deliberately exclude the spectra from these star formation regions. The significant strength of typically weak emission lines (such as [Cl III] λ5517Å and [Cl III] λ5537Å) and broad line features introduced significant fitting errors when attempting to fit the spectra with PPXF, since these features are not accounted for by PPXF.

4.3.6 *dw1244-1127*

dw1244-1127 is a star-forming dwarf irregular galaxy with a recessional velocity of $v_\odot = 2441 \pm 1\,\mathrm{km\,s^{-1}}$, placing it far in background behind M104, and thus is not a member of the M104 group. As shown in Fig. 10, this galaxy is likely a satellite of the nearby spiral galaxy NGC4680, with a velocity difference of $\Delta v = 25 \pm 1\,\mathrm{km\,s^{-1}}$.

4.4 Coherent satellite motion

Crosby et al. (2023b) hypothesized that LOS velocities alone may be sufficient to indicate the presence of a kinematic satellite plane, by comparing the mean value and width of the satellite LOS velocity distribution. If a stable plane consisting of coherently rotating satellites was observed at least partially face-on, then the expectation is that the LOS velocity distribution would appear abnormally cold for an environment of M104's mass, since the motions of each satellite would then be largely in the on-sky proper motions, rather than the LOS motions. Currently, we lack the means to acquire on-sky proper motions to directly reproduce the kinematics and determining highly precise (uncertainties less than ± 100 kpc) distances to satellites is difficult at the edge of the Local Volume where M104 resides.

We start by measuring the velocity dispersion of the likely M104 satellite members (Section 4.2) that have reliable radial velocities. To estimate the uncertainty in these velocities, we bootstrap the results, by randomly sub-sampling satellites with measured velocities allowing for replacement. Then, we compare these results to simulated M104 analogues from the cosmological simulation Illustris: The Next Generation 100 (Illustris TNG-100; Nelson et al. 2017; Pillepich et al. 2017; Springel et al. 2017; Marinacci et al. 2018; Naiman et al. 2018; Nelson et al. 2019). A total of 265 M104-like analogues were selected this way, as defined in Crosby et al. (2023b). We then selected groups using a friends of friends (FOF) groups that are separated from each other by at least 2 virial radii (R_{200}) and are selected based on the virial mass ($M_{200} = 10^{12}$–$10^{13}\,\mathrm{M_\odot}$) and the number of subhaloes ($n_{sub} = 30$–100) within the virial radius with at least an absolute g-band magnitude of $M_g = -9$. For each analogue, we select the 10 brightest satellites in the g-band (satellites as selected in Crosby et al. 2023b) and perform this same bootstrapping method to produce a velocity dispersion distribution for each simulated analogue, simulating a mock set of observations in a similar manner presented here for M104. All these distributions are then added together. We compared the LOS velocity dispersion distributions from simulated M104 analogues and M104 itself in

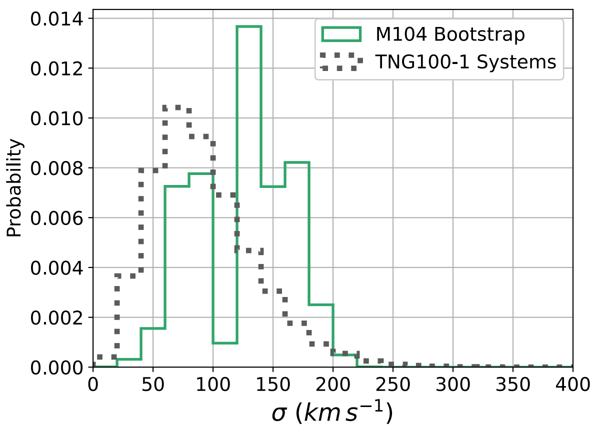

Figure 9. The distribution of the standard deviation of relative line-of-sight velocities for the bootstrapped sample of the M104 satellites with known recessional velocities (solid line) and the 265 similar M104 environments from the TNG100-1 simulation (dotted line). The mean velocity dispersions are $\sigma = 138 \pm 36\,\mathrm{km\,s^{-1}}$ and $\sigma = 92 \pm 43\,\mathrm{km\,s^{-1}}$ for the bootstrapped sample of M104 satellites and the M104 analogue systems in TNG100-1, respectively.

Fig. 9. From this process, we measure a mean satellite dispersion velocity of $\sigma = 92 \pm 43\,\mathrm{km\,s^{-1}}$ for M104-like analogues in Illustris TNG-100, and $\sigma = 138 \pm 36\,\mathrm{km\,s^{-1}}$ from our bootstrapped M104 satellites. Both distributions nearly lie within the $1\,\sigma$ of each other and thus we are unable to conclude that there exists the presence of unexpected coherent motion in the satellites in comparison to simulations.

However, this case only reveals the presence of a satellite plane when such a plane is largely face-on, where the satellite motion would be mostly in its on-sky proper motions relative to the observer and less of their true motion is detected in LOS velocities, thus the LOS velocity distribution appears to colder than less coherently rotating systems. In the case where it is edge-on, we can detect a satellite plane by measuring the fraction of satellites co-rotating in a disk around M104, and compare that to expectations from a non-planar system of satellites. Based on visual inspection of Fig. 10, there appears to be no preferential co-rotating axis yet, unlike other systems such as NGC4485/NGC4490 (Karachentsev & Kroupa 2024). But more likely, if a plane is present that can take any orientation, it will be somewhere between face-on and edge-on, and a number of other key parameters, such as the number of satellites in the plane and the plane thickness for example, could also vary significantly based on the diversity of satellite planes already known (Conn et al. 2013; Ibata et al. 2013; Müller et al. 2018a; Pawlowski & Kroupa 2019). Ultimately, this expanded analysis would involve comparing the shapes of the satellite LOS velocity distribution, more than just the collective dispersion. We currently lack enough measured recessional velocity from satellites to constrain the uncertainty of such an analysis, so we defer this analysis to later work.

4.5 Dynamical mass of M104

With the satellite velocity dispersion now measured, we can estimate the dynamical and baryonic mass of the M104 group. We can use the dynamical mass to compare to theoretical mass estimates from Crosby et al. (2023b). From the virial theorem we can use the velocity dispersion to calculate the total mass enclosed within a radius:

$$M_{\mathrm{tot}} = \frac{5 R_{\max} v_\sigma^2}{G}, \tag{5}$$

where v_σ^2 is the velocity dispersion as calculated above and R_{max} is the maximum radial extent of the satellite galaxies. For this value, we use the maximum projected radial extent of the satellites multiplied by $\sqrt{2}$, which is ~ 595 kpc. From this, we determine $M_{\mathrm{tot}} = (12.4 \pm 6.5) \times 10^{12}\mathrm{M}_\odot$, which is slightly higher than our theoretical mass estimate from Crosby et al. (2023b) of $7.8 \times 10^{12}\,\mathrm{M}_\odot$, calculated from the stellar mass of M104 and the average stellar mass to total halo mass ratio measured from the TNG100 simulation for similar M104-analogues as described in Section 4.4. This is in line with a similar dynamical mass measurement of $M_{\mathrm{tot}} = 15.5 \pm 4.9 \times 10^{12}\,\mathrm{M}_\odot$ from Karachentsev et al. (2020), which considered a larger number of dwarf galaxies up to ~ 1 Mpc away from M104.

The stellar mass of M104 is $M_* = 1.8 \times 10^{11}\,\mathrm{M}_\odot$ (Muñoz-Mateos et al. 2015) and likely dominates > 99 per cent of all stellar mass within the virial radius given its brightest satellite PGC42730 has a stellar mass of only $10^9\,\mathrm{M}_\odot$. The stellar masses of the next brightest satellites, among those quoted in Table 5, are even less significant. The baryonic mass fraction of the universe as measured by Aghanim et al. (2020) is expected to be $\Omega_b/\Omega_m \sim 0.16$ and we expect to find a similar ratio within the M104 system. This indicates that the total mass of baryons within M104's virial radius should be $M_{bary} = 2.0 \pm 1.0 \times 10^{12}\mathrm{M}_\odot$, based on the dynamical mass measurement above. The stellar mass of M104 is known and the baryonic mass of its satellites is negligible, so there should be a gas mass of $M_{gas} =\sim 1.8 \times 10^{12}\mathrm{M}_\odot$ within the virial radius. This indicates the gas to stellar mass ratio should be $M_{gas}/M_* \sim 10$ in order to satisfy the baryonic to dark matter mass ratio, but it is very unlikely that a galaxy such as M104 possess that much gas. A similar class of L_* galaxy Cen A possesses at most $M_{gas}/M_* \sim 0.2$ (Müller et al. 2022) and larger statistical analyses of L_* galaxies suggest that for a galaxy of M104's stellar mass, then this ratio is at most $M_{gas}/M_* \sim 0.3$ (Warren, Jerjen & Koribalski 2007; Parkash et al. 2018). This suggests that M104's baryonic mass to total mass ratio is much smaller than expected, by a factor of ~ 10. Karachentsev et al. (2020) noted a similar phenomenon with the stellar mass to total mass ratio, which was lower by a factor of ~ 10 for that analysis as well. Curiously, our TNG100 sample of simulated M104 analogues have a mean M_{gas}/M_* ratio of $M_{\mathrm{gas}}/M_* = 3.8 \pm 2.0$ for a mean stellar mass of $M_* = (0.9 \pm 0.4) \times 10^{11}\,\mathrm{M}_\odot$, which is consistently higher than that expected from observations (Warren et al. 2007; Parkash et al. 2018; Müller et al. 2022). However, this still falls short of the expected ratio from observations.

4.6 Mass–metallicity relation

We show the mass–metallicity relation for the newly observed M104 satellite galaxies in Fig. 11. We compare the M104 satellites to the dEs observed using MUSE in Heesters et al. (2023). We also plot the root mean square fit of the mass–metallicity relation for the Milky Way dwarfs from Kirby et al. (2013). Heesters et al. (2023) found that their sample of early-type dwarf galaxies were mostly more metal poor than the relation found from the Milky Way dwarfs. Here, we find that within 1σ uncertainty, our M104 dwarfs are consistent with the Milky Way trend. We note that some of spectra have low SNR (SNR < 20), which may produce biased stellar ages and metallicities (Woo et al. 2024) and thus we have shown these data points separately in Fig. 11. This suggests that the chemical evolution

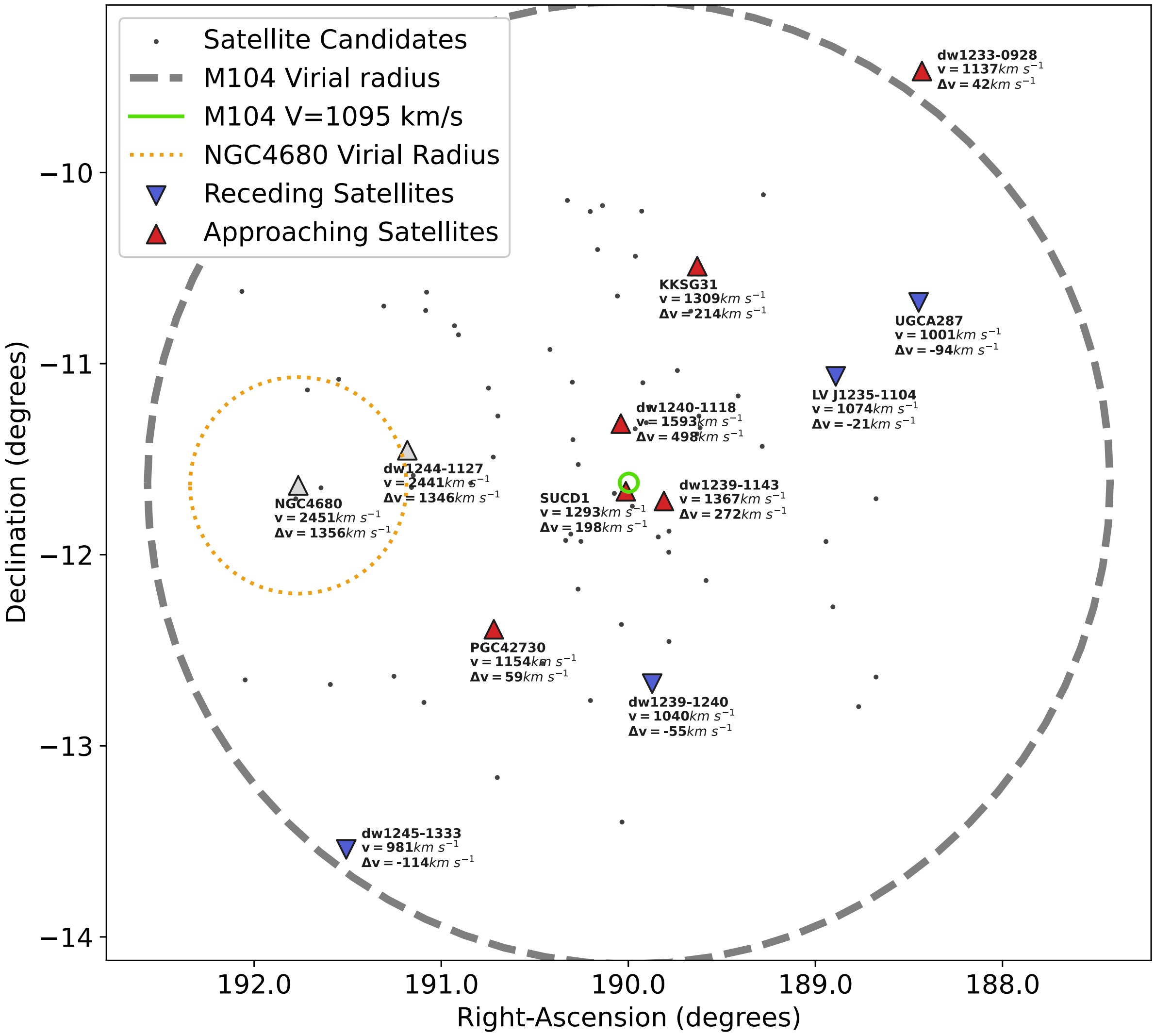

Figure 10. Galaxy distribution in the M104 group environment with measured satellite galaxy velocities. The nine satellites have a mean heliocentric velocity of 1156 km s^{-1} and a velocity dispersion of 221 km s^{-1}. Velocities relative to M104 (1094 km s^{-1}) are also given. Symbol colour and the direction of the triangular symbols reflects the relative velocity. As noted in Crosby et al. (2023b), the M104 environment is well defined in velocity space with a significant velocity gap of over 1000 km s^{-1} to the next galaxy grouping in the background that includes NGC4680 (2451 km s^{-1}). The dwarf dw1244-1127 (2426 km s^{-1}) is most likely a companion of NGC4680 as judged from its small relative velocity difference of 25 km s^{-1} and its proximity to NGC4680's virial radius.

of the M104 environment followed similar pathway as the Milky Way environment, despite the key differences, such as the abundance of dwarf satellites and the presence of nucleated dE galaxies.

5 SUMMARY AND CONCLUSION

In this paper, we have presented details spectroscopy of ten dwarf galaxies in the vicinity of M104, nine of which we can conclude are satellites of M104 based on recessional velocities alone. Of these nine dwarf galaxies, one is a BCD, two are dwarf irregular, five are nucleated dE galaxies, and one is a dE galaxy with no nucleus. The remaining background galaxy is a dwarf irregular.

These galaxies collectively span stellar masses 2×10^7 to 1×10^9 M$_\odot$. For the dEs, the mean mass weighted ages of these dwarf galaxies span the range $7.0 - 11.0$ Gyr with metallicities -1.7 to -0.3. The dwarf irregulars UGCA287, dw1233-0928 and dw1244-1127 follow similar trends with the exception of the presence of a younger stellar population. These ages and metallicities match expectations of the historical formation scenarios of dE and irregular galaxies, which suggest these galaxies collectively formed early in the universe, around $\sim 7 - 12$ Gyr ago.

This spectroscopy includes one BCD and candidate green pea, LV J1235-1104. This low-mass galaxy ($M_* = 8.4 \times 10^7$ M$_\odot$) has extreme emission features powered by star formation, the equivalent width of [O III] 5007 Å is 314 Å and we have detected broad components to emission lines with $\sigma \sim 250$ km s^{-1}, consistent with the spectral properties of higher redshift starburst dwarf galaxies named extreme emission-line galaxies (EELGs) or GPs. It is forming stars at a rate of 0.042 $M_\odot$ yr^{-1} as measured from the H_α flux, which gives it an sSFR of 5×10^{-10} yr^{-1} which however falls short of typical values for EELGs or GPs. This galaxy contains two powerful star-forming regions, whose intense radiation field is producing a galactic outflow of hot ionized gas filling the circumgalactic medium about this galaxy, and optical emission features are visible in our spectra up to ~ 1 kpc away from the star formation regions. The similarity of this galaxies unique emission features to those of GPs

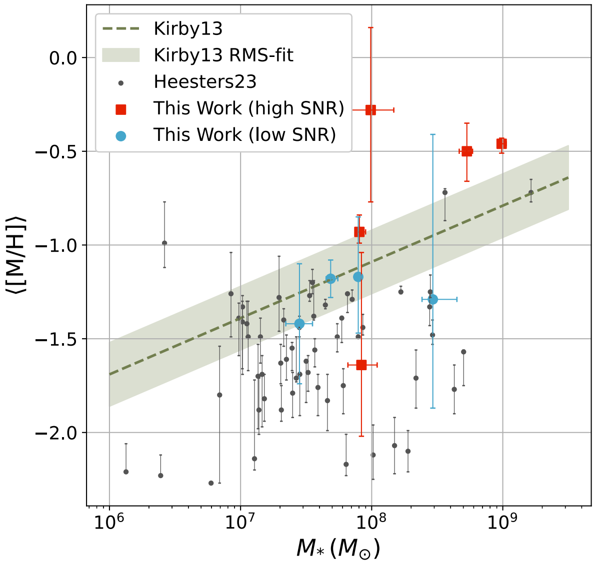

Figure 11. The mass–metallicity relation of the satellites of M104 as presented here, split between those with high SNR (> 20, shown with squares) and low SNR (≤ 20, shown with large circles), the sample of dE galaxies from Heesters et al. (2023) (small circles) and the root mean square fit of the mass–metallicity relation for Milky Way dwarf satellites from Kirby et al. (2013).

makes this galaxy a candidate Ly α/Ly C photon leaking galaxy, like higher redshift starburst galaxies. This class of galaxy in the Local Volume is exceedingly rare, and are not usually satellite galaxies, making this satellite particularly unique. As with most low-mass starburst dwarf galaxies it is not immediately obvious what triggered this galaxy's starburst, but given that environmental interactions are likely to rapidly strip a low-mass galaxy of this kind of its star-forming gas, it is likely a recent addition to the M104 system of satellites.

We consider the bulk recessional velocities of these galaxies in the context of satellite planes. By comparing the dispersion in of the LOS velocities sample of M104 satellites producing by bootstrapping to that of simulated M104 analogues in the Illustris TNG100-1 simulation, we find no significant difference between the two, indicating that a satellite plane that contends with ΛCDM simulations of the kind around the Milky Way, M31, or Cen A is not currently detected around M104. However, with only 10 out of 70 possible satellite candidates around M104 within the virial radius confirmed with spectroscopy, ongoing observations and re-testing of this hypothesis will be required.

Finally, we use our new recessional velocities to measure the dynamical mass of M104 within the virial radius. We measure a mass of $M_{\rm tot} = (12.4 \pm 6.5) \times 10^{12}\,{\rm M}_\odot$ and thus a revised virial radius of $R_{vir} = 491 \pm 86$ kpc. Considering M104's stellar mass ($M_{*,M104} = 1.8 \times 10^{11} {\rm M}_\odot$), the likely gas content for an M104-like galaxy ($M_{gas} \sim 0.25\, M_*$), indicates that >90 per cent of its expected baryons are missing, given expected baryon mass fractions from cosmological observations. This matches similar findings from prior measurements of M104's dynamical mass, and of Cen A (Müller et al. 2021), a morphologically similar galaxy to M104.

ACKNOWLEDGEMENTS

MSP acknowledges funding via a Leibniz-Junior Research Group (project number J94/2020).

IE acknowledges generous support from a Carnegie-Princeton Fellowship through Princeton University.

DATA AVAILABILITY

The data underlying this article will be shared on reasonable request to the corresponding author.

REFERENCES

Aghanim N. et al., 2020, A&A, 641, A6
Amorín R. O., Muñoz Tuñón C., Aguerri J. A. L., Cairós L. M., Caon N., 2007, A&A, 467, 541
Amorín R., Pérez-Montero E., Vílchez J. M., Papaderos P., 2012, ApJ, 749, 185
Amorín R. et al., 2015, A&A, 578, A105
Anand G. S., Tully R. B., Rizzi L., Shaya E. J., Karachentsev I. D., 2019, ApJ, 880, 52
Aragon-Calvo M. A., Silk J., Neyrinck M., 2022, MNRAS, 520, L28
Bahl H., Baumgardt H., 2014, MNRAS, 438, 2916
Banik I., Thies I., Truelove R., Candlish G., Famaey B., Pawlowski M. S., Ibata R., Kroupa P., 2022, MNRAS, 513, 129
Bílek M., Thies I., Kroupa P., Famaey B., 2018, A&A, 614, A59
Bosch G. et al., 2019, MNRAS, 489, 1787
Brunker S. W., Salzer J. J., Kimsey-Miller B., Cousins B., 2022, ApJ, 926, 131
Buck T., Dutton A. A., Macciò A. V., 2016, MNRAS, 460, 4348
Byun W. et al., 2020, ApJ, 891, 18
Calzetti D. et al., 2007, ApJ, 666, 870
Cappellari M., 2016, MNRAS, 466, 798
Cappellari M., 2023, MNRAS, 526, 3273
Cappellari M., Emsellem E., 2004, PASP, 116, 138
Cardamone C. et al., 2009, MNRAS, 399, 1191
Carlsten S. G., Greco J. P., Beaton R. L., Greene J. E., 2020, ApJ, 891, 144
Carlsten S. G., Greene J. E., Beaton R. L., Danieli S., Greco J. P., 2022, ApJ, 933, 47
Cautun M., Bose S., Frenk C. S., Guo Q., Han J., Hellwing W. A., Sawala T., Wang W., 2015, MNRAS, 452, 3838
Conn A. R. et al., 2013, ApJ, 766, 120
Corwin Harold G. J., Buta R. J., de Vaucouleurs G., 1994, AJ, 108, 2128
Crnojević D. et al., 2016, ApJ, 823, 19
Crosby E., Jerjen H., Müller O., Pawlowski M., Mateo M., Dirnberger M., 2023a, MNRAS, 521, 4009
Crosby E., Jerjen H., Müller O., Pawlowski M. S., Mateo M., Lelli F., 2023b, MNRAS, 527, 9118
Curti M. et al., 2022, MNRAS, 518, 425
Danieli S. et al., 2020, ApJ, 894, 119
Davidson R., Flachaire E., 2008, J. Econom., 146, 162
Faber S. M., Balick B., Gallagher J. S., Knapp G. R., 1977, ApJ, 214, 383
Fahrion K. et al., 2022, A&A, 667, A101
Flury S. R. et al., 2022, ApJS, 260, 1
Garavito-Camargo N., Patel E., Besla G., Price-Whelan A. M., Gómez F. A., Laporte C. F. P., Johnston K. V., 2021, ApJ, 923, 140
Garrison-Kimmel S. et al., 2019, MNRAS, 489, 4574
Geha M., Guhathakurta P., van der Marel R. P., 2003, AJ, 126, 1794
Gillet N., Ocvirk P., Aubert D., Knebe A., Libeskind N., Yepes G., Gottlöber S., Hoffman Y., 2015, ApJ, 800, 34
Hammer F., Yang Y., Fouquet S., Pawlowski M. S., Kroupa P., Puech M., Flores H., Wang J., 2013, MNRAS, 431, 3543
Harish S. et al., 2022, ApJ, 934, 167
Hau G. K. T., Spitler L. R., Forbes D. A., Proctor R. N., Strader J., Mendel J. T., Brodie J. P., Harris W. E., 2009, MNRAS, 394, L97
Heesters N. et al., 2021, A&A, 654, 15
Heesters N. et al., 2023, A&A, 676, A33
Hogarth L. et al., 2020, MNRAS, 494, 3541
Huchtmeier W. K., Karachentsev I. D., Karachentseva V. E., 2009, A&A, 506, 677

Ibata R. A. et al., 2013, Nature, 493, 62
Ibata R. A., Ibata N. G., Lewis G. F., Martin N. F., Conn A., Elahi P., Arias V., Fernando N., 2014, ApJ, 784, L6
Izotov Y. I., Schaerer D., Worseck G., Guseva N. G., Thuan T. X., Verhamme A., Orlitová I., Fricke K. J., 2017, MNRAS, 474, 4514
Izotov Y. I., Worseck G., Schaerer D., Guseva N. G., Thuan T. X., Fricke, Verhamme A., Orlitová I., 2018, MNRAS, 478, 4851
Javanmardi B. et al., 2016, A&A, 588, 89
Jones D. H. et al., 2009, MNRAS, 399, 683
Karachentsev I. D., Kaisin S. S., 2020, MNRAS, 495, 3592
Karachentsev I. D., Kroupa P., 2024, MNRAS, 528, 2805
Karachentsev I. D., Karachentseva V. E., Suchkov A. A., Grebel E. K., 2000, A&ASS, 145, 415
Karachentsev I. D., Tully R. B., Makarova L. N., Makarov D. I., Rizzi L., 2015, ApJ, 805, 144
Karachentsev I. D., Makarova L. N., Tully R. B., Anand G. S., Rizzi L., Shaya E. J., 2020, A&A, 643, A124
Kirby E. N., Cohen J. G., Guhathakurta P., Cheng L., Bullock J. S., Gallazzi A., 2013, ApJ, 779, 102
Komarova L., Oey M. S., Krumholz M. R., Silich S., Kumari N., James B. L., 2021, ApJ, 920, L46
Kourkchi E., Tully R. B., 2017, ApJ, 843, 16
Kroupa P., 2001, MNRAS, 322, 231
Kroupa P., 2012, Publ. Astron. Soc. Aust., 29, 395
Kroupa P., Theis C., Boily C. M., 2005, A&A, 431, 517
Krumholz M. R., Matzner C. D., 2009, ApJ, 703, 1352
Laufman L., Scarlata C., Hayes M., Skillman E., 2022, ApJ, 940, 31
Lee J. C., Kennicutt R. C., Funes S. J. J. G., Sakai S., Akiyama S., 2009, ApJ, 692, 1305
Lewis B. M., 1985, ApJ, 292, 451
Libeskind N. I., Knebe A., Hoffman Y., Gottlöber S., Yepes G., Steinmetz M., 2010, MNRAS, 411, 1525
Libeskind N. I. et al., 2019, MNRAS, 490, 3786
Liu S. et al., 2022, ApJ, 927, 57
Lovell M. R., Eke V. R., Frenk C. S., Jenkins A., 2011, MNRAS, 413, 3013
Malkan M. A., Malkan B. K., 2021, ApJ, 909, 92
Marinacci F. et al., 2018, MNRAS, 480, 5113
Martínez-Delgado D. et al., 2021, A&A, 652, A48
Mateo M., Bailey J. I., Crane J., Shectman S., Thompson I., Roederer I., Bigelow B., Gunnels S., 2012, in McLean I. S., Ramsay S. K., Takami H., eds, Proc. SPIE Conf. Ser. Vol. 8446, Ground-based and Airborne Instrumentation for Astronomy IV. SPIE, Bellingham, p. 84464Y
Mateo M., Bailey J. I., Song Y.-Y., Crane J. D., Hull C., Shectman S., Birk C., 2022, in Evans C. J., Bryant J. J., Motohara K., eds, Proc. SPIE Conf. Ser. Vol. 12184, Ground-based and Airborne Instrumentation for Astronomy IX. SPIE, Bellingham, p. 121845P
McCall M. L., 2014, MNRAS, 440, 405
McQuinn K. B. W., Skillman E. D., Dolphin A. E., Berg D., Kennicutt R., 2016, AJ, 152, 144
Metz M., Kroupa P., 2007, MNRAS, 376, 387
Metz M., Kroupa P., Jerjen H., 2009a, MNRAS, 394, 2223
Metz M., Kroupa P., Theis C., Hensler G., Jerjen H., 2009b, ApJ, 697, 269
Miller C. J., Stark A., Gifford D., Kern N., 2016, ApJ, 822, 41
Müller O., Jerjen H., 2020, A&A, 644, A91
Müller O., Scalera R., Binggeli B., Jerjen H., 2017, A&A, 602, A119
Müller O., Pawlowski M. S., Jerjen H., Lelli F., 2018a, Science, 359, 534
Müller O., Jerjen H., Binggeli B., 2018b, A&A, 615, A105
Müller O., Rejkuba M., Pawlowski M. S., Ibata R., Lelli F., Hilker M., Jerjen H., 2019, A&A, 629, A18
Müller O. et al., 2021, A&A, 645, L5
Müller O., Lelli F., Famaey B., Pawlowski M. S., Fahrion K., Rejkuba M., Hilker M., Jerjen H., 2022, A&A, 662, A57
Muñoz-Mateos J. C. et al., 2015, ApJS, 219, 3
Naiman J. P. et al., 2018, MNRAS, 477, 1206
Nelson D. et al., 2017, MNRAS, 475, 624
Nelson D. et al., 2019, Comput. Astrophys. Cosmol., 6, 2
Neuzil M. K., Mansfield P., Kravtsov A. V., 2020, MNRAS, 494, 2600
Parkash V., Brown M. J. I., Jarrett T. H., Bonne N. J., 2018, ApJ, 864, 40
Pawlowski M. S., 2018, Mod. Phys. Lett., 33, 1830004
Pawlowski M. S., 2021, Nat. Astron., 5, 1185
Pawlowski M. S., Kroupa P., 2019, MNRAS, 491, 3042
Pawlowski M. S., Sohn S. T., 2021, ApJ, 923, 42
Pawlowski M. S., Pflamm-Altenburg J., Kroupa P., 2012, MNRAS, 423, 1109
Pawlowski M. S., McGaugh S. S., Jerjen H., 2015, MNRAS, 453, 1047
Pietrinferni A., Cassisi S., Salaris M., Castelli F., 2004, ApJ, 612, 168
Pillepich A. et al., 2017, MNRAS, 473, 4077
Putman M. E., Zheng Y., Price-Whelan A. M., Grcevich J., Johnson A. C., Tollerud E., Peek J. E. G., 2021, ApJ, 913, 53
Retana-Montenegro E., Van Hese E., Gentile G., Baes M., Frutos-Alfaro F., 2012, A&A, 540, A70
Rhoads J. E. et al., 2023, ApJ, 942, L14
Romano M. et al., 2023, A&A, 677, A44
Samuel J., Wetzel A., Chapman S., Tollerud E., Hopkins P. F., Boylan-Kolchin M., Bailin J., Faucher-Giguère C.-A., 2021, MNRAS, 504, 1379
Schweizer F., 1978, ApJ, 220, 98
Sen S. et al., 2017, MNRAS, 475, 3453
Sen S., Peletier R. F., Vazdekis A., 2022, MNRAS, 515, 3472
Shao S., Cautun M., Frenk C. S., 2019, MNRAS, 488, 1166
Simpson C. M., Grand R. J. J., Gómez F. A., Marinacci F., Pakmor R., Springel V., Campbell D. J. R., Frenk C. S., 2018, MNRAS, 478, 548
Springel V. et al., 2017, MNRAS, 475, 676
Storey P. J., Hummer D. G., 1995, MNRAS, 272, 41
Taylor A. J., Barger A. J., Cowie L. L., 2022, ApJ, 939, L3
Trump J. R. et al., 2023, ApJ, 945, 35
Tully R. B., 1982, ApJ, 257, 389
Tully R. B., Shaya E. J., Karachentsev I. D., Courtois H. M., Kocevski D. D., Rizzi L., Peel A., 2008, ApJ, 676, 184
Tully R. B., Libeskind N. I., Karachentsev I. D., Karachentseva V. E., Rizzi L., Shaya E. J., 2015, ApJ, 802, L25
Tully R. B., Courtois H. M., Sorce J. G., 2016, AJ, 152, 50
Vasiliev E., 2023, MNRAS, 527, 437
Vazdekis A., Koleva M., Ricciardelli E., Röck B., Falcón-Barroso J., 2016, MNRAS, 463, 3409
Warren B. E., Jerjen H., Koribalski B. S., 2007, AJ, 134, 1849
Wetzel A. R., Tollerud E. J., Weisz D. R., 2015, ApJ, 808, L27
Woo J., Walters D., Archinuk F., Faber S. M., Ellison S. L., Teimoorinia H., Iyer K., 2024, MNRAS, 530, 4260
Yang H., Malhotra S., Rhoads J. E., Wang J., 2017, ApJ, 847, 38
Zhao Y., Gu Q., Gao Y., 2011, AJ, 141, 68
Zou H. et al., 2017, PASP, 129, 064101
Zou H. et al., 2018, ApJS, 237, 37

This paper has been typeset from a TEX/LATEX file prepared by the author.